Photothermal radiometry parametric identifiability theory for reliable and unique nondestructive coating thickness and thermophysical measurements

X. Guo, A. Mandelis, J. Tolev, and K. Tang

Citation: Journal of Applied Physics **121**, 095101 (2017); doi: 10.1063/1.4977246
View online: http://dx.doi.org/10.1063/1.4977246
View Table of Contents: http://aip.scitation.org/toc/jap/121/9
Published by the American Institute of Physics

JOURNAL OF APPLIED PHYSICS **121**, 095101 (2017)

Photothermal radiometry parametric identifiability theory for reliable and unique nondestructive coating thickness and thermophysical measurements

X. Guo,[a] A. Mandelis, J. Tolev, and K. Tang
Center for Advanced Diffusion-Wave and Photoacoustic Technologies (CADIPT), Department of Mechanical and Industrial Engineering, University of Toronto, 5 King's College Road, Toronto, Ontario M5S 3G8, Canada

(Received 4 January 2017; accepted 12 February 2017; published online 1 March 2017)

In this paper, we present a detailed reliability analysis of estimated parameters to a three-layer theoretical model of photothermal radiometry frequency domain signals by applying parameter identifiability conditions from two steel samples coated with $\sim$10 μm and 20 μm thick ceramic coating, to measure the thermophysical parameters of the coating, such as thermal diffusivity, thermal conductivity, and coating thickness. The three parameters are unique only when their sensitivity coefficients are linearly independent over the range of measurements. The study demonstrates the complexity of the identifiable experimental conditions through identifiability maps (calculated nonidentifiable locations) and sensitivity coefficient plots, even when the three separated parameters are grouped into two parameters. The validation of the reliability analysis theory by comparing the independently measured, with the fitted thicknesses of two coatings under random and optimized conditions, underscore the great importance of identifiability analysis (sensitivity coefficient plots) in the design of experiments for reliable parameter extractions, especially when the number of parameters is greater than the measurement data channels. *Published by AIP Publishing.* [http://dx.doi.org/10.1063/1.4977246]

I. INTRODUCTION

Photothermal radiometry (PTR) is an important nondestructive testing/evaluation (NDT/E) methodology. Its non-contact nature makes it especially appealing for industrial component parameter measurements. Since it was first introduced in 1979,[1] PTR has been applied to the measurement of thermophysical and optical properties of materials such as thermal diffusivity, thermal conductivity, and optical absorption coefficient.[2–7] The quantification of thermal and optical parameters is usually achieved by fitting experimental data to a theoretical model, and measurements depend on the type of laser source (frequency-modulated or pulsed PTR) and material structures (layered or bulk). The accuracy of the fitted parameters is judged by the goodness of fit. However, best fitting may yield different values of the same parameters. For example, Busse and Walther reported the thermal diffusivity of copper[8] measured using thermal wave techniques by three different measurement groups.[9–11] The derived values were 1.3×10^{-4} m^2/s, 1.15×10^{-4} m^2/s, and 1.11×10^{-4} m^2/s. The difference was as high as 18%, and this raises questions of reliability of multi-parameter estimations. It is thus of significance to investigate the conditions under which multi-parameters can be uniquely estimated. The uniqueness of estimated parameters belongs to the identifiability problem of well-established parameter estimations in engineering and science.[12] It has been shown that parameters in a function can be simultaneously estimated if the sensitivity coefficients, the first derivatives of the function with respect to the parameters, over the range of the observations are not linearly dependent. That identifiability criterion constitutes a guide to which parameters or groups of parameters can be uniquely estimated and are, therefore, reliable. Careful design of experiments by means of identifiability analysis can save unnecessary time and imprecise measurements by avoiding the problem of non-identifiability. The sensitivity and error in the multi-parameter determination were investigated in the past.[13–15] However, to our best knowledge, no detailed, systematic identifiability analysis of photothermal best fitting practices has ever been performed to offer a general guide to the problem of reliability and uniqueness in photothermal measurements which has always been a challenge, since the number of unknown parameters is greater than the number of the measurement channels. In this paper, we address the reliability, and thus the uniqueness, of thermophysical and physical property measurements (thermal diffusivity, thermal conductivity, and coating thickness) by developing the identifiability conditions for frequency-domain photothermal radiometry (PTR) signals (amplitude and phase) from a three-layer model. The paper answers the following three questions: (1) Are the parameters identifiable (linearly independent)? (2) What are their sensitivities, if they are identifiable? (3) In what observation (such as frequency) ranges are the parameters sensitive? The identifiability analysis is then validated by fitting amplitudes and phases of PTR signals from measurements made on two ceramic-coated steel samples.

II. THEORY

A. Three-layer model

A one-dimensional photothermal model for a three-layered structure was introduced in a previous paper.[5] Figure 1 shows the geometry of the model consisting of a roughness equivalent-layer (thickness L_1, thermal diffusivity α_1, and

[a]E-mail: guox@mie.utoronto.ca

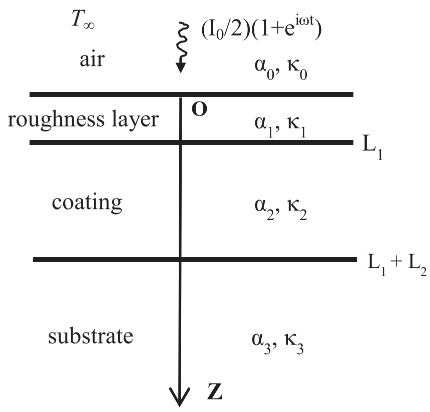

FIG. 1. One dimension three-layer model.

thermal conductivity κ_1), coating layer (thickness L_2, thermal diffusivity α_2, and thermal conductivity κ_2), and substrate layer (thickness $L_3 \rightarrow \infty$, thermal diffusivity α_3, and thermal conductivity κ_3). The multilayered arrangement is irradiated with a broad laser beam of sinusoidally modulated intensity I_o at frequency f. In the backscattered mode, the radiometric signal $\Delta T_1(0, f)$ (the oscillating temperature field on the surface) of an opaque solid can be written as[16]

$$\Delta T_1(0,f) = \frac{(1-R_1)I_0(1-\gamma_{01})}{2\kappa_1\sigma_1}\left(\frac{1+\rho_{321}e^{-2\sigma_1 L_1}}{1-\rho_{321}e^{-2\sigma_1 L_1}}\right), \quad (1)$$

where

$$\rho_{321} = -\gamma_{21}\left[\frac{1+(\gamma_{32}/\gamma_{21})e^{-2\sigma_2 L_2}}{1+(\gamma_{32}\gamma_{21})e^{-2\sigma_2 L_2}}\right], \quad (2)$$

$$\sigma_m = (1+i)\sqrt{\frac{\pi f}{\alpha_m}}; \quad \gamma_{mn} \equiv \frac{b_{mn}-1}{b_{mn}+1}; \quad b_{mn} = \frac{\kappa_m\sqrt{\alpha_n}}{\kappa_n\sqrt{\alpha_m}}. \quad (3)$$

m, $n = 0, 1, 2, 3$ refers to air, roughness layer, coating layer, and substrate. R_1 is the reflectance of the roughness layer, where the light absorption occurs.

Usually the signal from Eq. (1) is normalized with a signal from a reference sample, for example, the bare substrate, to remove the instrumental effects. The lock-in amplifier signal will be normalized and expressed as

$$\Delta T_{1N}(0,f) = \frac{\Delta T_1(0,f)}{\Delta T_3(0,f)} = \frac{(1-R_1)}{(1-R_s)}\frac{\kappa_1\sigma_1}{\kappa_3\sigma_3}\frac{(1-\gamma_{01})}{(1-\gamma_{03})}\left(\frac{1+\rho_{321}e^{-2\sigma_1 L_1}}{1-\rho_{321}e^{-2\sigma_1 L_1}}\right). \quad (4)$$

where R_s is the reflection coefficient of the substrate.

If the parameters α, κ, and L are grouped together as follows:

$$Q_m = \frac{L_m}{\sqrt{\alpha_m}}; \quad P_m = \frac{\kappa_m}{\sqrt{\alpha_m}}. \quad (5)$$

Eq. (4) becomes

$$\Delta T_{1N}(0,f) = \frac{(1-R_1)P_3(1-\gamma_{01})}{(1-R_s)P_1(1-\gamma_{03})}\left(\frac{1+\rho_{321}e^{-2(1+i)\sqrt{\pi f}Q_1}}{1-\rho_{321}e^{-2(1+i)\sqrt{\pi f}Q_1}}\right), \quad (6)$$

where ρ_{321}, γ_{21}, and γ_{32} can be written as

$$\rho_{321} = -\gamma_{21}\left[\frac{1+(\gamma_{32}/\gamma_{21})e^{-2(1+i)\sqrt{\pi f}Q_2}}{1+(\gamma_{32}\gamma_{21})e^{-2(1+i)\sqrt{\pi f}Q_2}}\right]; \quad \gamma_{21} = \frac{P_2-P_1}{P_2+P_1}; \quad \gamma_{32} = \frac{P_3-P_2}{P_3+P_2}. \quad (7)$$

If b_{mn} in Eq. (3) is written in terms of P_m, P_n

$$b_{mn} = \frac{P_m}{P_n}. \quad (8)$$

then, Eq. (6) can be rewritten as

$$\Delta T_{1N}(0,f) = b_{31}\frac{(1-R_1)(1-\gamma_{01})}{(1-R_s)(1-\gamma_{03})}\left(\frac{1+\rho_{321}e^{-2(1+i)\sqrt{\pi f}Q_1}}{1-\rho_{321}e^{-2(1+i)\sqrt{\pi f}Q_1}}\right). \quad (9)$$

where γ_{21} and γ_{32} in ρ_{321} can be written as

$$\gamma_{21} = \frac{b_{21}-1}{b_{21}+1}; \quad \gamma_{32} = \frac{b_{32}-1}{b_{32}+1}.$$

The signals corresponding to Eqs. (4), (6), and (9) can be demodulated through a lock-in amplifier and expressed as amplitude A and phase P

$$A = \sqrt{X^2+Y^2}, \quad P = \tan^{-1}\left(\frac{Y}{X}\right). \quad (10)$$

X and Y are the real and imaginary parts of ΔT_{1N}, respectively. Note the factor $\frac{(1-R_1)}{(1-R_s)}$ in Eq. (6) is a constant and only affects the absolute value of amplitude (which is not very important in experiments with instrumental effects), and therefore was simplified as 1 in this paper. This factor does not affect the phase which is a ratio of two signals (quadrature and in-phase), each of which is multiplied by it, so it cancels out.

B. Multi-parameter identifiability

1. Sensitivity coefficients

The sensitivity coefficient S_i is defined as the first derivative of the function η with respect to parameter β_i

$$S_i = \frac{\partial_\eta}{\partial \beta_i}. \quad (11)$$

For Eq. (4), the separate parameters to be estimated are α_2, κ_2, and L_2. The related sensitivity coefficients for amplitude and phase are

$$S_s(A) = \left[\frac{\partial A(f)}{\partial \alpha_2} \quad \frac{\partial A(f)}{\partial \kappa_2} \quad \frac{\partial A(f)}{\partial L_2}\right],$$
$$S_s(P) = \left[\frac{\partial P(f)}{\partial \alpha_2} \quad \frac{\partial P(f)}{\partial \kappa_2} \quad \frac{\partial P(f)}{\partial L_2}\right]. \tag{12}$$

For Eq. (6), the grouped parameters are Q_2 and P_2, and the related sensitivity coefficients are

$$S_{g1}(A) = \left[\frac{\partial A(f)}{\partial Q_2} \quad \frac{\partial A(f)}{\partial P_2}\right],$$
$$S_{g1}(P) = \left[\frac{\partial P(f)}{\partial Q_2} \quad \frac{\partial P(f)}{\partial P_2}\right]. \tag{13}$$

For Eq. (9), the grouped parameters are Q_2 and b_{32} and the related sensitivity coefficients are

$$S_{g2}(A) = \left[\frac{\partial A(f)}{\partial Q_2} \quad \frac{\partial A(f)}{\partial b_{32}}\right], \quad S_{g2}(P) = \left[\frac{\partial P(f)}{\partial Q_2} \quad \frac{\partial P(f)}{\partial b_{32}}\right]. \tag{14}$$

2. Identifiability conditions

The multi-parameter identifiability condition is that all the parameters should be linearly independent over the range of observations. Linear dependence occurs when for p parameters, the relation[12]

$$C_1\frac{\partial \eta_i}{\partial \beta_1} + C_2\frac{\partial \eta_i}{\partial \beta_2} + \cdots C_p\frac{\partial \eta_i}{\partial \beta_p} = 0 \tag{15}$$

is true for all i observations provided not all the C_j values are equal to zero. Eq. (15) is satisfied if, and only if, the determinant of the $p \times p$ matrix formed by the sensitivity coefficients is zero

$$detS = \begin{vmatrix} \frac{\partial \eta_1}{\partial \beta_1} & \cdots & \frac{\partial \eta_1}{\partial \beta_p} \\ \vdots & \ddots & \vdots \\ \frac{\partial \eta_p}{\partial \beta_1} & \cdots & \frac{\partial \eta_p}{\partial \beta_p} \end{vmatrix} = 0. \tag{16}$$

The identifiability criterion for the three-layered model is thus derived as follows:

For separate parameters (α_2, κ_2, L_2)

$$detS_s(A) = \begin{vmatrix} \frac{\partial A(f_1)}{\partial \alpha_2} & \frac{\partial A(f_1)}{\partial \kappa_2} & \frac{\partial A(f_1)}{\partial L_2} \\ \frac{\partial A(f_2)}{\partial \alpha_2} & \frac{\partial A(f_2)}{\partial \kappa_2} & \frac{\partial A(f_2)}{\partial L_2} \\ \frac{\partial A(f_3)}{\partial \alpha_2} & \frac{\partial A(f_3)}{\partial \kappa_2} & \frac{\partial A(f_3)}{\partial L_2} \end{vmatrix} \neq 0, \tag{17}$$

$$detS_s(P) = \begin{vmatrix} \frac{\partial P(f_1)}{\partial \alpha_2} & \frac{\partial P(f_1)}{\partial \kappa_2} & \frac{\partial P(f_1)}{\partial L_2} \\ \frac{\partial P(f_2)}{\partial \alpha_2} & \frac{\partial P(f_2)}{\partial \kappa_2} & \frac{\partial P(f_2)}{\partial L_2} \\ \frac{\partial P(f_3)}{\partial \alpha_2} & \frac{\partial P(f_3)}{\partial \kappa_2} & \frac{\partial P(f_3)}{\partial L_2} \end{vmatrix} \neq 0; \tag{18}$$

for grouped parameters (Q2, P2)

$$detS_{g1}(A) = \begin{vmatrix} \frac{\partial A(f_1)}{\partial Q_2} & \frac{\partial A(f_1)}{\partial P_2} \\ \frac{\partial A(f_2)}{\partial Q_2} & \frac{\partial A(f_2)}{\partial P_2} \end{vmatrix} \neq 0, \tag{19}$$

$$detS_{g1}(P) = \begin{vmatrix} \frac{\partial P(f_1)}{\partial Q_2} & \frac{\partial P(f_1)}{\partial P_2} \\ \frac{\partial P(f_2)}{\partial Q_2} & \frac{\partial P(f_2)}{\partial P_2} \end{vmatrix} \neq 0; \tag{20}$$

and for grouped parameter (Q_2, b_{32})

$$detS_{g2}(A) = \begin{vmatrix} \frac{\partial A(f_1)}{\partial Q_2} & \frac{\partial A(f_1)}{\partial b_{32}} \\ \frac{\partial A(f_2)}{\partial Q_2} & \frac{\partial A(f_2)}{\partial b_{32}} \end{vmatrix} \neq 0, \tag{21}$$

$$detS_{g2}(P) = \begin{vmatrix} \frac{\partial P(f_1)}{\partial Q_2} & \frac{\partial P(f_1)}{\partial b_{32}} \\ \frac{\partial P(f_2)}{\partial Q_2} & \frac{\partial P(f_2)}{\partial b_{32}} \end{vmatrix} \neq 0, \tag{22}$$

where (f_1, f_2, f_3) are three different modulation frequencies.

III. RESULTS AND DISCUSSION

A. Simulation results

Simulations were based on ceramic coated steel samples with different coating thicknesses. They were performed by calculating the sensitivity coefficients and the determinants of the sensitivity coefficient matrices ((Eqs. (12)–(22)) and evaluating them with the known parameter values (obtained from literature and the manufacturer) in Table I and the unknown parameter ranges (estimated from our previous measurements) in Table II. A large modulation frequency span $f = 1$–2000 Hz was used to check the identifiable parameter range.

1. Separate parameters

a. Identifiability. Checking the condition of linear independence of the sensitivity coefficients is a convenient way to determine if the multi-parameters are identifiable under the measurement conditions. Figure 2 shows the 40×40 identifiability maps of amplitude (Figure 2(a)) and phase (Figure 2(b)) with fixed α_2 and κ_2 values (1.5×10^{-6} m^2/s and 4.1 W/mK) while the modulation frequency f spans the 1 to 2000 Hz range and the coating thickness L_2 varies from 1 μm to 30 μm. The black diamonds in the figure indicate the locations where the identifiability condition is not met, e.g., the three parameters are linearly dependent (zero determinant of the sensitivity coefficients matrix). It can be seen that the parameter identifiability is strongly influenced by modulation frequency and coating thickness range. For amplitude, the best regions for the entire modulation range are coating thicknesses below 5 μm and above 25 μm. There is also a window at coating thickness around 15 μm. For other coating thickness regions, only parts of the modulation frequency

TABLE I. Values of known parameters used in simulations.

	Separate parameters			Grouped parameters		
Layer number j	α_j (m^2/s)	κ_j (W/mK)	L_j (m)	Q_j ($s^{1/2}$)	P_j ($Ws^{1/2}/m^2K$)	b_{01}, b_{03}, b_{31},
0	22.6×10^{-6}	0.026			5.5	8.3×10^{-5}
1	1.65×10^{-6}	84.4	1×10^{-6}	0.78×10^3	6.57×10^4	7.8×10^{-4}
3	3.9×10^{-6}	14			7×10^3	0.11

TABLE II. Ranges of unknown parameters used in simulations.

Separate parameters			Grouped parameters		
α_2 (m^2/s)	κ_2 (W/mK)	L_2 (m)	Q_2 ($s^{1/2}$)	P_2 ($Ws^{1/2}/m^2K$)	b_{32}
$(0.3–2.7) \times 10^{-6}$	0.83–7.49	$(1–30) \times 10^{-6}$	$(3.26–29) \times 10^{-3}$	$(0.68–6.11) \times 10^3$	0.42−3.76

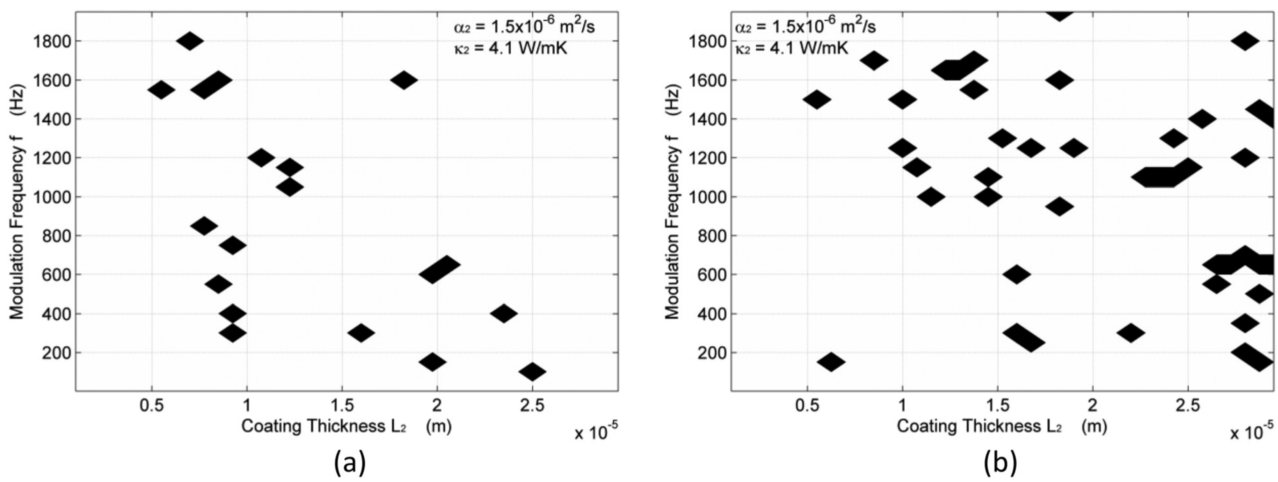

FIG. 2. Calculated linearly dependent points as a function of modulation frequency f and coating thickness L_2 at $\alpha_2 = 1.5 \times 10^{-6}$ m^2/s and $\kappa_2 = 4.1$ W/mK. (a) amplitude; (b) phase.

range are identifiable. For example, at a coating thickness of 20 μm, only the region above 700 Hz is identifiable. Compared with the amplitude identifiability map, the phase map contains more linearly dependent points. The best regions are below 15 μm and below 1000 Hz. However, there is also a window around 20 μm.

Figure 3 displays the identifiability maps of amplitude (Figure 3(a)) and phase (Figure 3(b)) with fixed modulation

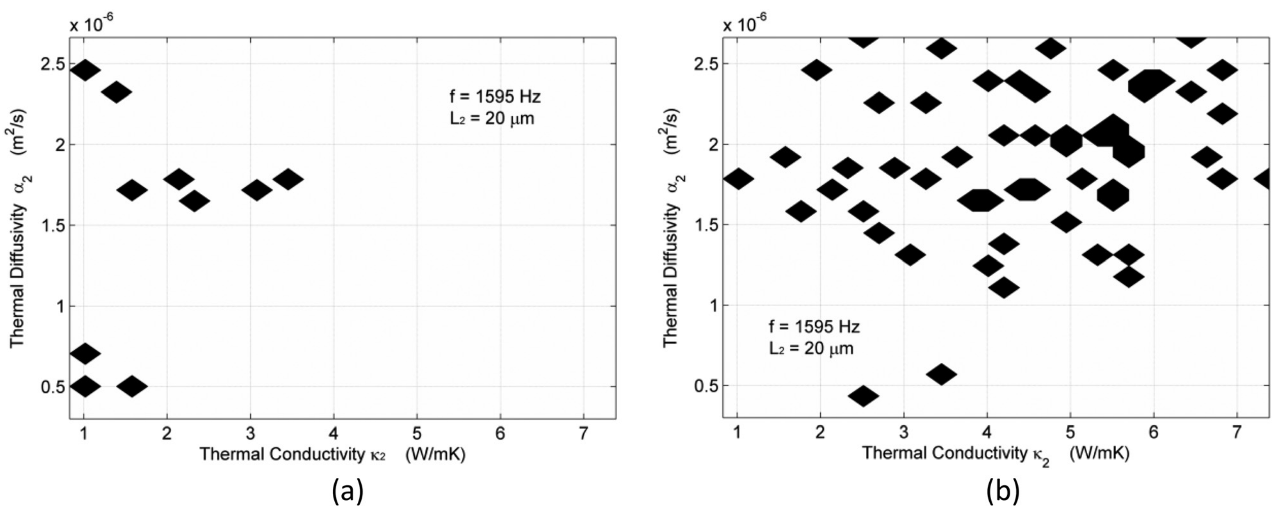

FIG. 3. Calculated linearly dependent points as a function of thermal diffusivity α_2 and thermal conductivity κ_2 at modulation frequency $f = 1595$ Hz and coating thickness $L_2 = 20$ μm. (a) amplitude; (b) phase.

frequency f and coating thickness L_2 values (1595 Hz and 20 μm) and with α_2 and κ_2 varying from 0.3×10^{-6} m^2/s to 2.7×10^{-6} m^2/s and from 0.83 W/mK to 7.49 W/mK, respectively. It is shown that the amplitude identifiability is low at low κ_2 value regions (<4 W/mK). For phase, the identifiability is high at low α_2 values (<1×10^{-6} m^2/s).

Figures 2 and 3 demonstrate that parameter identifiability is influenced by several factors, not only by measurement conditions (modulation frequency) and sample geometry (coating thickness), but also by the thermophysical property range.

b. Sensitivity coefficients. Even if parameters are linearly independent, the sensitivity of the parameters is also very important in their estimation. Illustrated in Fig. 4 are the parameter sensitivity coefficient maps as functions of modulation frequency f (1–2000 Hz) and coating thickness L_2 (1–30 μm) calculated at $\alpha_2 = 1.5 \times 10^{-6}$ m^2/s; $\kappa_2 = 4.1$ W/mK. Figures 4(a), 4(b), and 4(c) are α_2, κ_2, and L_2 sensitivity coefficient maps of amplitude, respectively. Figures 4(d)–4(f) are the corresponding phase maps. The maps exhibit very complex sensitivity distributions under different conditions. For illustration purposes, some typical sensitivity coefficient curves are extracted from the maps in Fig. 4 and presented in Figs. 5 and 6. Figure 5 shows how the parameter sensitivity coefficients of amplitude ((a), (b), (c)) and phase ((d), (e), (f)) change with modulation frequency at three coating thicknesses $L_2 = 30$ μm, 20 μm, and 9 μm. It is noticed that both

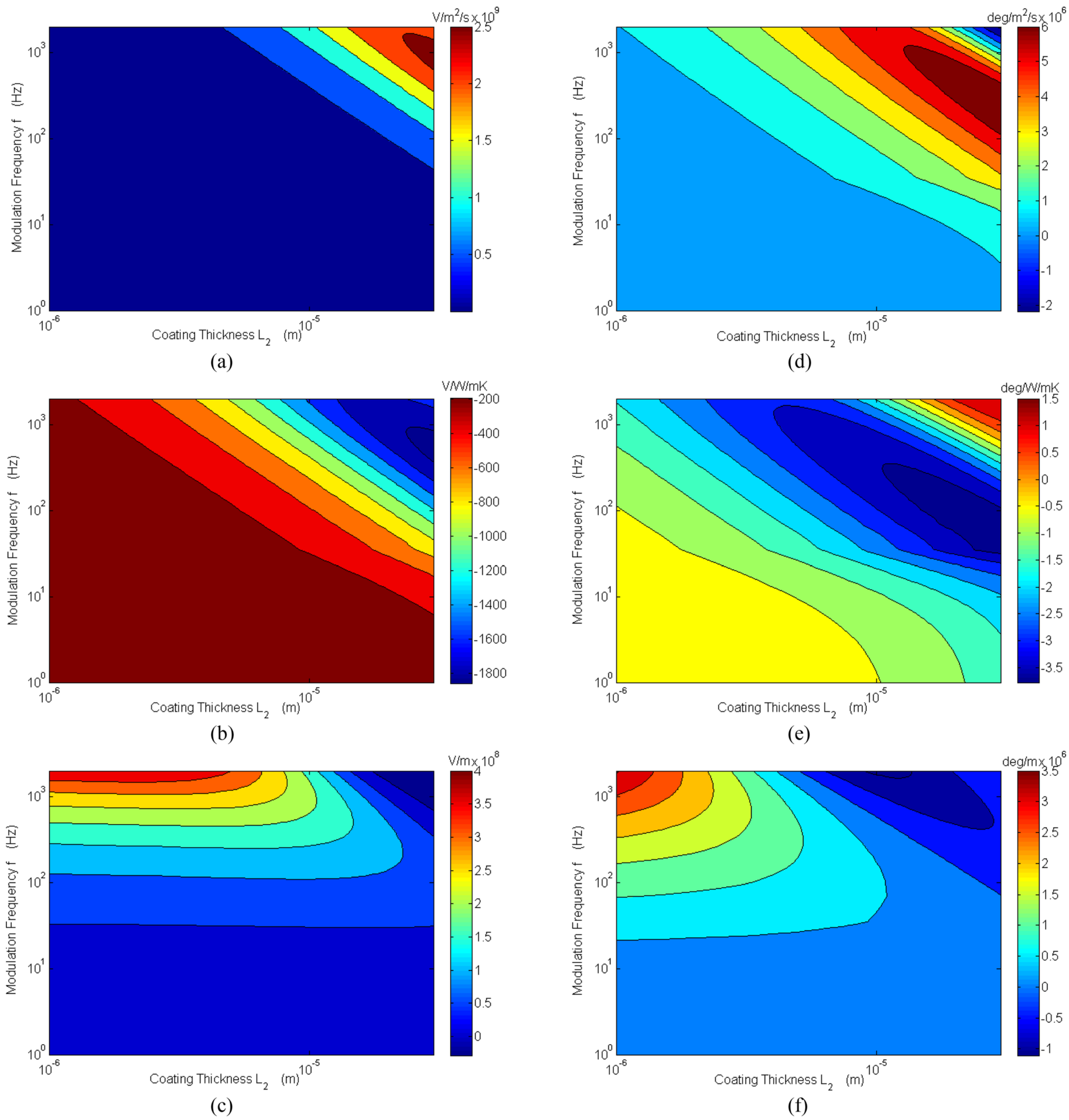

FIG. 4. Calculated parameter sensitivity coefficients (at $\alpha_2 = 1.5 \times 10^{-6}$ m^2/s; $\kappa_2 = 4.1$ W/mK) as a function of modulation frequency f and coating thickness L_2. (a)–(c) are α_2, κ_2, and L_2 sensitivity coefficient maps of amplitude. (d)–(f) are α_2, κ_2, and L_2 sensitivity coefficient maps of phase.

magnitude and sign of the sensitivity coefficients can change with modulation frequency. In Figs. 5(a) (amplitude) and 5(d) (phase), the sensitivity coefficient curves of α_2 increase with a modulation frequency first, with higher sensitivity for thicker coatings, and then reverse at some 'critical' frequencies, which are ∼300 Hz (30 μm), 600 Hz (20 μm), and 2000 Hz (9 μm) for phase in Fig. 5(d). Compared with the phase, the amplitude sensitivity coefficient curve maxima appear at

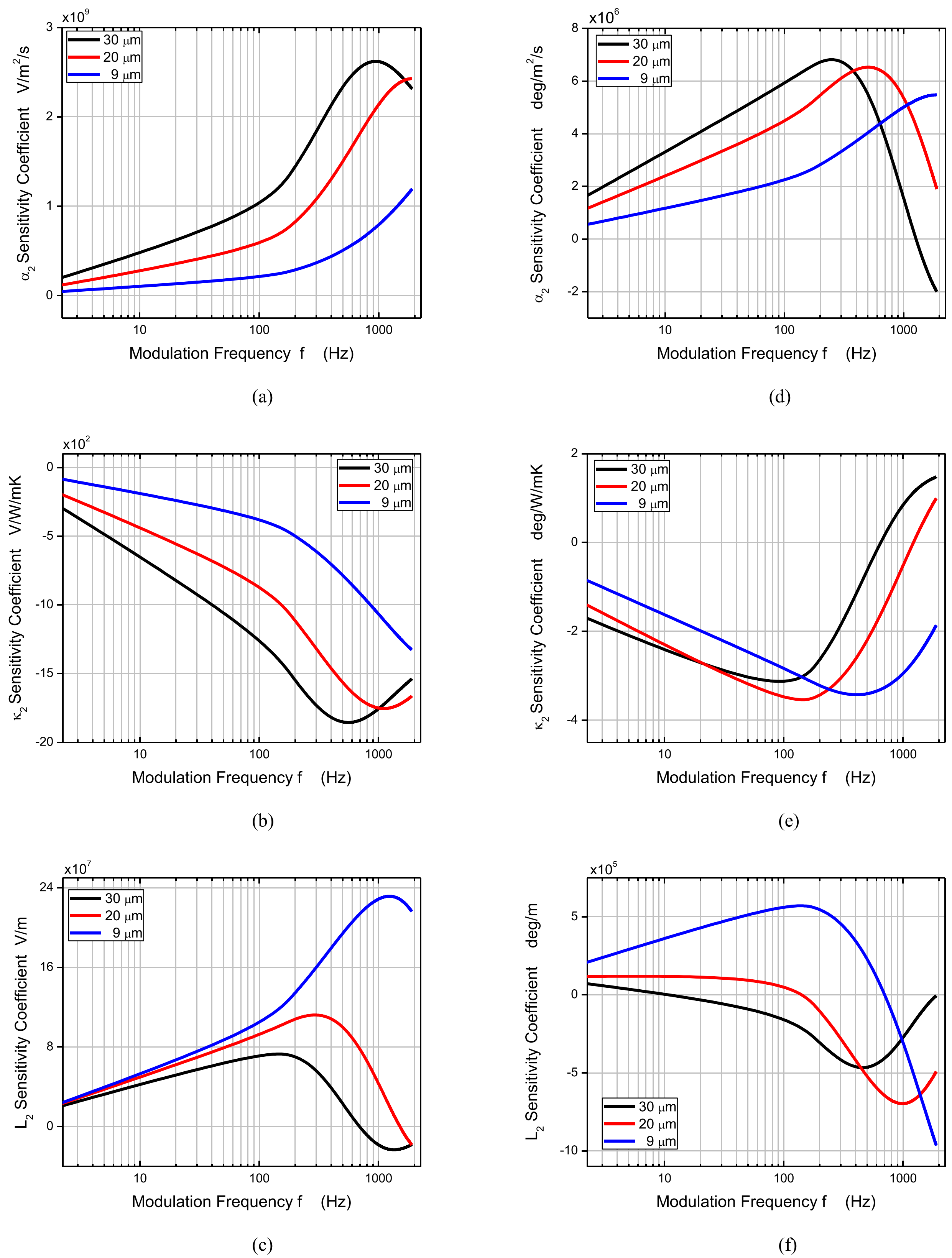

FIG. 5. Calculated parameter sensitivity (at $\alpha_2 = 1.5 \times 10^{-6}$ m^2/s; $\kappa_2 = 4.1$ W/mK) as a function of frequency f at three different coating thicknesses $L_2 = 30\,\mu$m, 20 μm, and 9 μm. (a)–(c) are amplitude sensitivity coefficient curves for α_2, κ_2, and L_2; (d)–(f) are the corresponding phase curves.

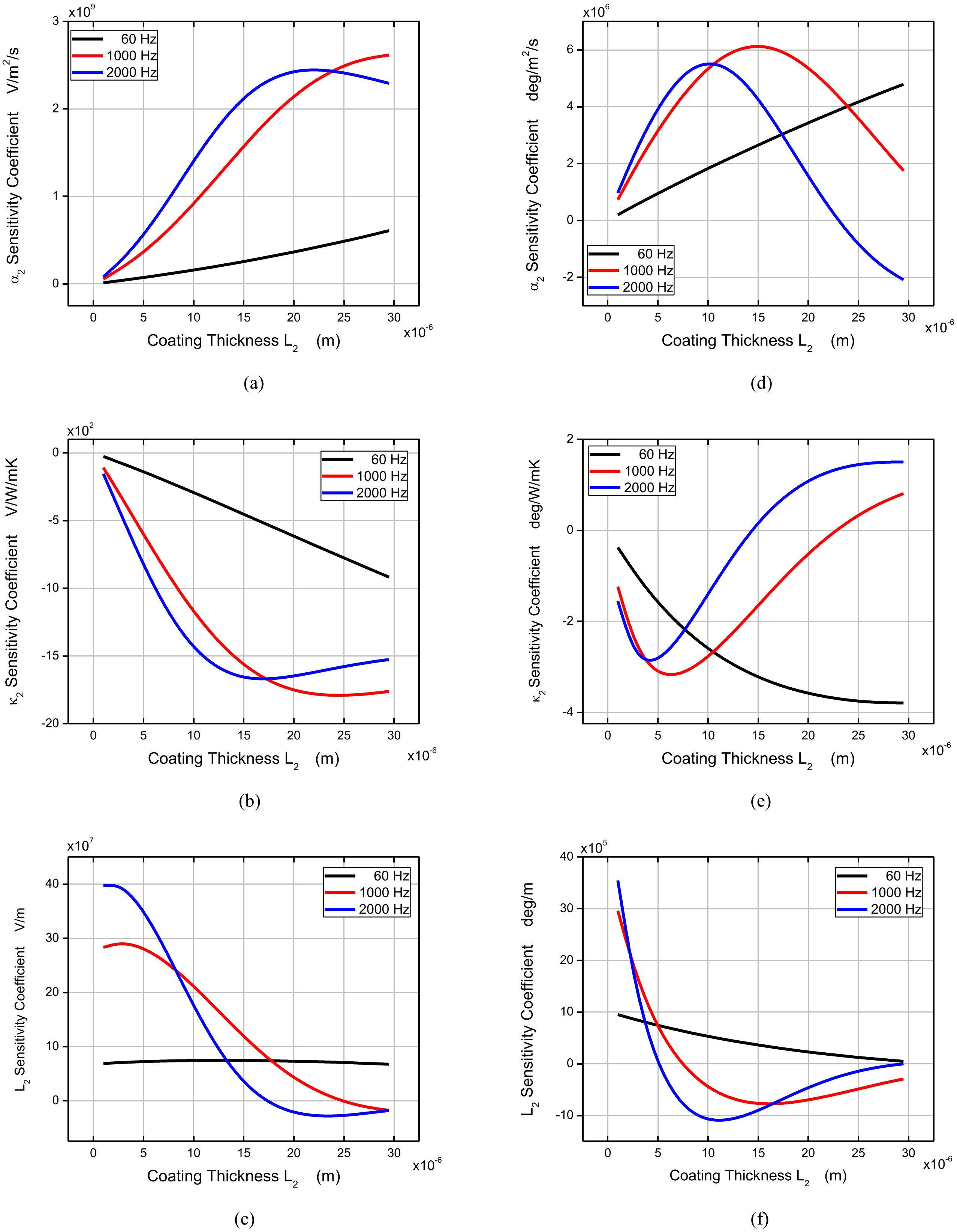

FIG. 6. Calculated parameter sensitivity (at $\alpha_2 = 1.5 \times 10^{-6}$ m^2/s; $\kappa_2 = 4.1$ W/mK) as a function of coating thickness L_2 at three different modulation frequencies $f = 60$ Hz, 1000 Hz, and 2000 Hz. (a)–(c) are amplitude sensitivity coefficient curves for α_2, κ_2, and L_2; (d)–(f) L_2 are the corresponding phase curves.

relatively higher frequencies, 1000 Hz (30 μm) (versus 300 Hz in phase). Considering Fig. 5(e), the phase sensitivity coefficient curve $L_2 = 30\,\mu$m of κ_2, as an example, the sensitivity coefficient increases with a modulation frequency first with negative sign (meaning the phase signal responds reversely with κ_2), reaching maximum sensitivity around 100 Hz, then decreasing to its minimum (zero), and increasing again with a positive sign above 600 Hz. Zero sensitivity indicates that κ_2

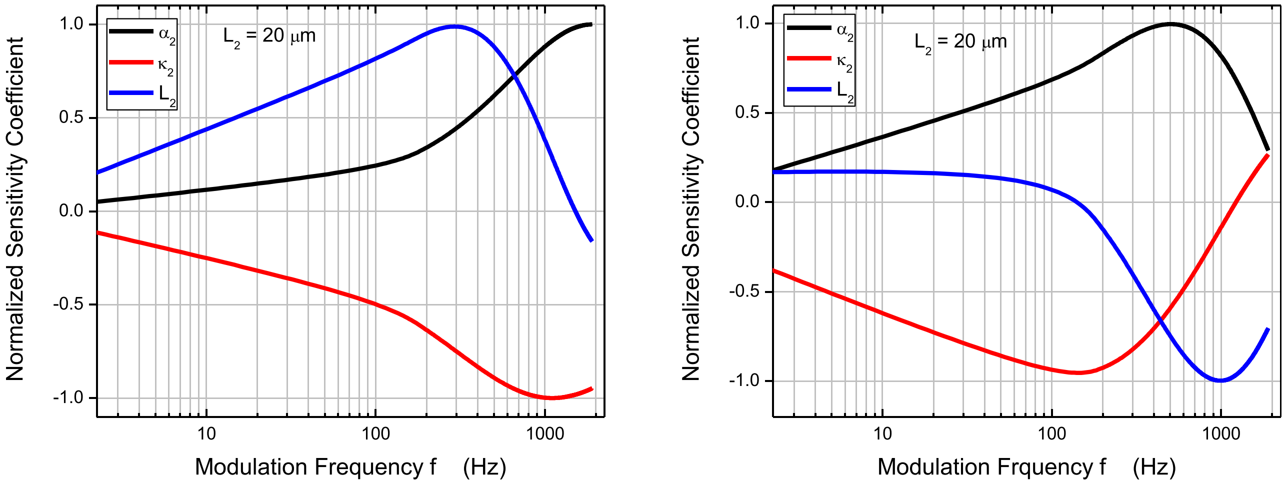

(a) (b)

FIG. 7. Normalized parameter sensitivity coefficients (at $\alpha_2 = 1.5 \times 10^{-6}$ m^2/s; $\kappa_2 = 4.1$ W/mK) as a function of modulation frequency at coating thickness $L_2 = 20\,\mu$m. (a) amplitude; (b) phase.

is unidentifiable at this position. If the whole modulation frequency range is used in the experiments and in data fitting, the *averaged* sensitivity of κ_2 will be greatly compromised due to the contributions from zero and the opposite sensitivity frequency ranges. The optimal frequency range should be 40–200 Hz. However, the optimal frequency range will shift upwards with a decrease of coating thickness, with $L_2 = 20\,\mu$m toward the middle and with $L_2 = 9\,\mu$m toward the highest frequency range. It is also observed that the sensitivity coefficient order of magnitude at different coating thicknesses changes with a modulation frequency: the thickest coating exhibits a higher sensitivity below 10 Hz; the thinnest coating has a higher sensitivity above 300 Hz; and the intermediate range for the $L_2 = 20\,\mu$m coating. Compared with the phase, the amplitude κ_2 sensitivity coefficient curves, Fig. 5(b), look simpler: they almost monotonically increase with modulation frequency, with maximum sensitivity occurring at progressively increasing frequencies as the coating thickness decreases. This is consistent with the decreasing thermal diffusion length probing thinner layers at higher frequencies. For L_2, the sensitivity coefficient curves, Fig. 5(c), exhibit opposite trends from α_2 and κ_2 below the 'critical' frequencies: the thinner the coating, the higher the sensitivity. The pattern of curves in Fig. 5(f) is more complicated, and the optimal frequency windows are very narrow (300 Hz–400 Hz and 900 Hz–1000 Hz) for 30 and 20 μm, respectively.

Figure 6 shows how the parameter sensitivity coefficients of amplitude ((a)–(c)) and phase ((d)–(f)) change with coating thickness at three modulation frequencies $f = 60$ Hz, 1000 Hz, and 2000 Hz. Forα_2, the sensitivity coefficient curves of amplitude, Fig. 6(a), increase almost monotonically with coating thickness, with higher sensitivity at higher frequencies (1000 Hz and 2000 Hz). However, the phase sensitivity coefficient curves, Fig. 6(d), are not monotonic at high frequencies (1000 Hz and 2000 Hz): They increase with coating thickness below 10 μm and begin to reverse the trend above that

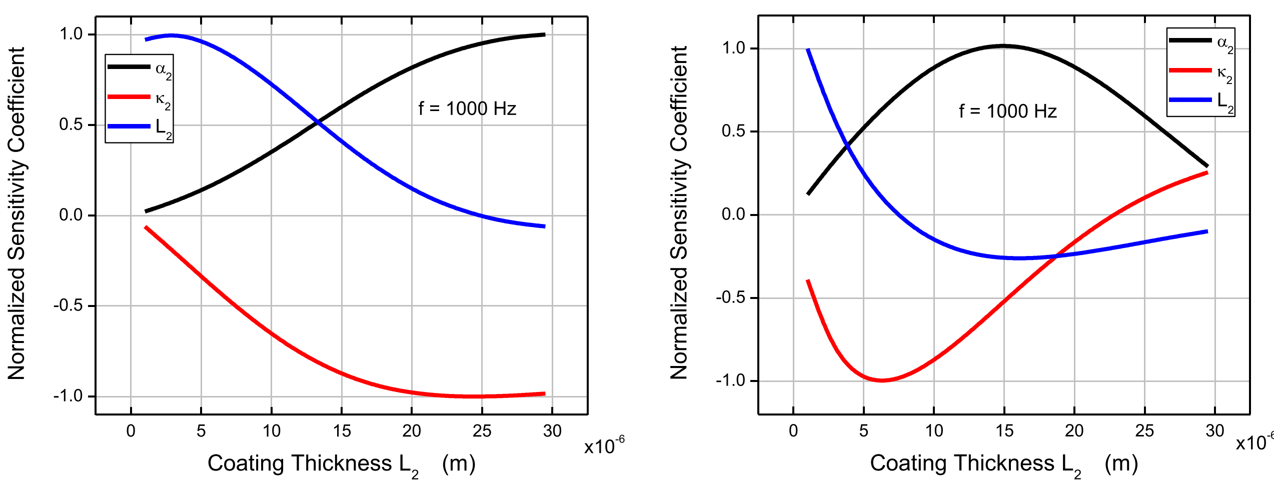

(a) (b)

FIG. 8. Normalized parameter sensitivity coefficients (at $\alpha_2 = 1.5 \times 10^{-6}$ m^2/s; $\kappa_2 = 4.1$ W/mK) as a function of coating thickness L_2 at modulation frequency $f = 1000$ Hz. (a) amplitude; (b) phase.

thickness. The sensitivity coefficient curves of κ_2, Figs. 6(b) and 6(e), show a similar pattern to the curves of α_2, but with opposite signs. For the amplitude sensitivity coefficient curves of L_2, Fig. 6(c), the thinner coatings (below 15 μm) have a higher sensitivity at the high frequencies (1000 Hz and 2000 Hz) and the thicker coating (above 15 μm) has a higher sensitivity at the low frequency (60 Hz), as expected intuitively from the well-known properties of thermal waves. For the phase, Fig. 6(f), at the low frequency (60 Hz), the sensitivity decreases with increasing coating thickness. At high frequencies (1000 Hz and 2000 Hz), the sensitivity is very high for coating thickness below 5 μm and relatively high between 10 μm and 15 μm. The sensitivity is gradually lost at all frequencies when the coating thickness approaches 30 μm, effectively becoming thermally semi-infinite.

For multi-parameter estimations, an optimal measurement condition should be found for all three parameters, α_2, κ_2, and L_2 because the maximum sensitivity position is not unique. The selection criterion is that the chosen frequency range must be one in which all three parameters have sensitivities close to their maxima. Figures 7 and 8 display the normalized sensitivity coefficient curves (positive maxima normalized to 1 and negative minima normalized to -1) for the three parameters $\alpha_2 = 1.5 \times 10^{-6}$ m^2/s; $\kappa_2 = 4.1$ W/mK and $L_2 = 20\,\mu$m as functions of modulation frequency and coating thickness, respectively. In Fig. 7, the optimal frequency range is around 200 Hz–600 Hz for both amplitude and phase. Figure 8 shows what sensitivity coefficient combinations could be obtained in different coating thickness regions if the modulation frequency is 1000 Hz. This figure indicates that the coating thickness range for best combined sensitivities to thermophysical properties might be 12 μm for amplitude and 5 μm for phase.

c. Amplitude and phase parameter sensitivity comparison. One of the advantages of frequency-domain measurements over pulsed PTR is the two-channel detection through amplitude and phase. In order to take full advantage of it, the parameter sensitivity of amplitude and phase should be compared. As an illustration, Fig. 9 displays the percent change in both

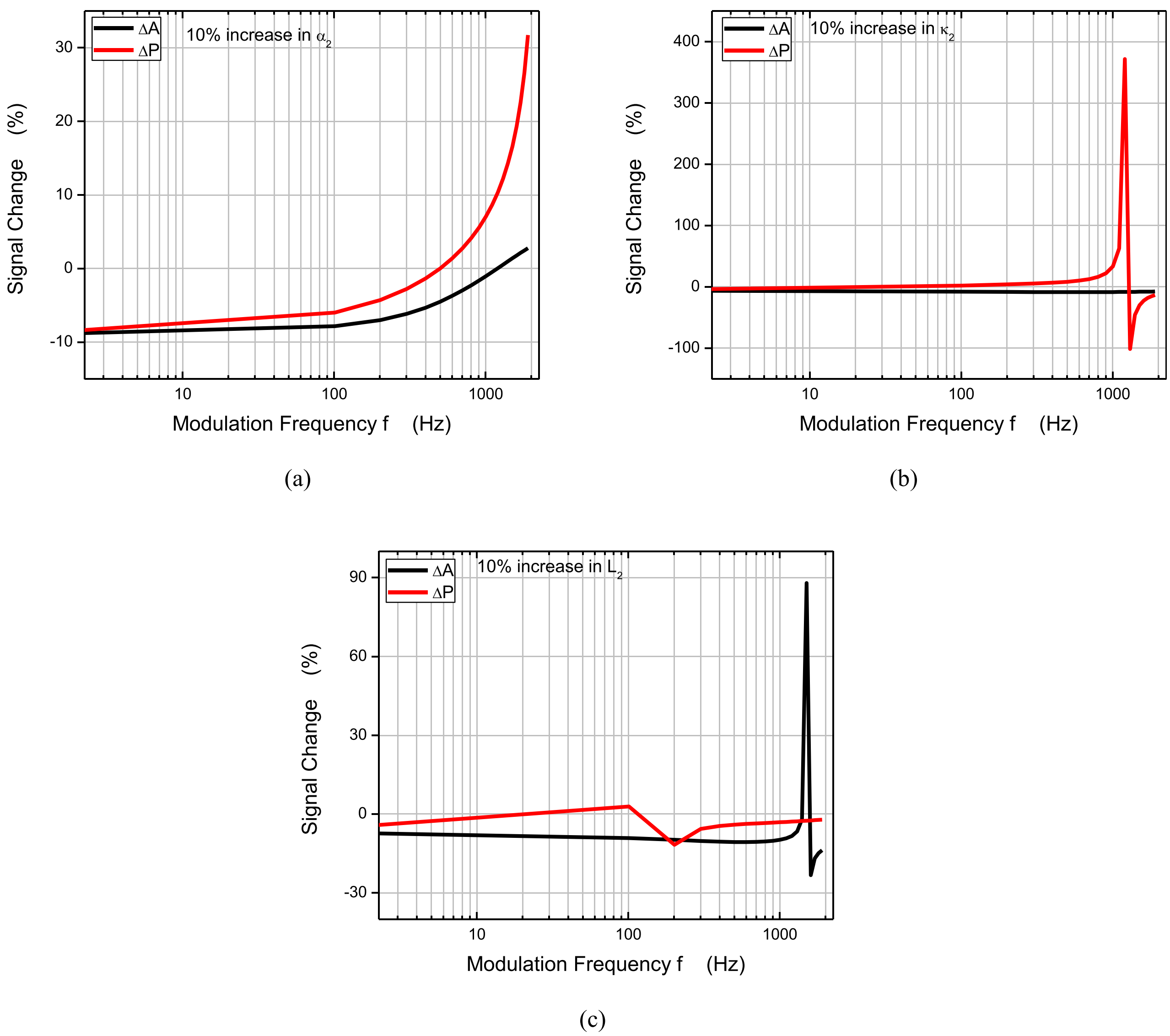

FIG. 9. Parameter sensitivity comparison between two signal channels, amplitude A and phase P, at $L_2 = 20\,\mu$m as a function of modulation frequency. Relative signal change, ΔA and ΔP, is due to 10% change in parameters (a) α_2; (b) κ_2; (c) L_2.

amplitude and phase as a function of modulation frequency when the three parameters (α_2, κ_2, L_2) increase by 10%, respectively. The signal changes ΔA and ΔP are calculated using the following equations:

$$\Delta A = \left\{\left[\beta(2)\times\frac{\partial A}{\partial\beta}(2)\right]-\left[\beta(1)\times\frac{\partial A}{\partial\beta}(1)\right]\right\} \times 100\Big/\left[\beta(1)\times\frac{\partial A}{\partial\beta}(1)\right], \tag{23}$$

$$\Delta P = \left\{\left[\beta(2)\times\frac{\partial P}{\partial\beta}(2)\right]-\left[\beta(1)\times\frac{\partial P}{\partial\beta}(1)\right]\right\} \times 100\Big/\left[\beta(1)\times\frac{\partial P}{\partial\beta}(1)\right]. \tag{24}$$

where $\beta(1)(\alpha_2, \kappa_2, L_2)$ represents $\alpha_2(1) = 1.5\times10^{-6}$ m^2/s, $\kappa_2(1) = 4.1$ W/mK, and $L_2(1) = 20\,\mu$m $\beta(2) = 1.1\beta(1)$.

Figure 9(a) shows that the amplitude is more sensitive than phase to α_2 below 700 Hz, while the phase sensitivity increases greatly above 1000 Hz. There are two 'blind' frequencies, where the amplitude and phase are insensitive, 500 Hz for P and 1000 Hz for A. Figure 9(b) shows that phase sensitivity to κ_2 increases faster above 700 Hz, but there is a steep drop due to sign change above 1000 Hz. Figure 9(c) exhibits the highest amplitude sensitivity to L_2 ($\sim$10% signal change) as compared to α_2 ($\sim$8% signal change) and κ_2 (<8% signal change) in the entire frequency range, not including the double sign change between 1000 Hz and 2000 Hz. The causes of the spikes occurring around $f = 1000$ Hz in the signal change induced by κ_2, Fig. 9(b), and L_2, Fig. 9(c) are the high relative sensitivity changes as a result of the denominators in Eqs. (23) and (24) becoming small due to very low absolute sensitivity values in this frequency range.

2. Grouped parameters

Unlike separate parameters, the calculated determinants of sensitivity matrices of grouped parameters (Q_2, P_2) and (Q_2, b_{32}) are all non-zero in the same frequency and coating thickness range and in the grouped parameter range as listed in Table II (the maps are not shown here). This indicates a high identifiability of the grouped parameters compared with separate parameters (Figs. 2 and 3). Figure 10 displays some typical sensitivity coefficient curves of the two grouped parameters (Q_2: (a) and (d), P_2: (b) and (e), b_{32}: (c) and (f)) as functions of modulation frequency for the three different coating thicknesses 9 μm, 20 μm, and 30 μm. Even though the unidentifiable locations are not found from the calculated determinants of the sensitivity coefficient matrices, the change of sign of the sensitivity coefficient curves implies the existence of unidentifiable locations because the curves must pass through zero values before they change their signs. This contradiction can be explained due to the low resolution of the 40×40 identifiability maps. On the other hand, it demonstrates the importance of sensitivity coefficient plots in the identifiability analysis. They can provide the whole identifiability picture of a parameter in terms of sensitivity. Because any zero sensitivity value from the paired parameters will compromise their identifiability, we can see that for the amplitudes ((a),(b), and (c)), the unidentifiable locations appear only at high frequencies, above 200 Hz, while the phase unidentifiable regions vary from parameter to parameter: for the 20 and 30 μm coatings, they occur across the low modulation frequency range <200 Hz in Fig. 10(d); at high frequencies above 1000 Hz in Fig. 10(f), and are identifiable at all frequencies for 9, 20, and 30 μm in Fig. 10(e). Figure 10 reveals that even for the grouped parameters, the identifiable range is limited. Special care is still required when taking these plots into account in the selection of the optimal experimental conditions. The common optimal frequency range appears to be 100 Hz–200 Hz for amplitude and phase.

B. Simulation validation—A case study

1. Materials and method

Two ceramic-coated steel samples with different coating thicknesses, labeled *thin* and *thick*, were measured in this study. The manufacturer's data sheet provided a total coating thickness ($L = L_1 + L_2$) as follows: *thin*: 9.7 ± 0.8 μm, *thick*: 20.6 ± 0.6 μm. Figure 11 shows the microscope images of cross-sections of the two coated samples. The roughness equivalent-layer thickness L_1 was outside our measurement frequency range and was assumed to be 1 μm-thick in this study.

The experimental setup of the PTR system used in this study is shown in Fig. 12. The modulated beam from a diode laser (Jenoptik, Germany) of 808 nm wavelength, $\sim$3-mm diameter beam size and $\sim$2-W power irradiated the sample through a beam steering mirror. The IR thermal photon flux (PTR signal) was collected and focused on a two-stage-thermoelectrically cooled MCZT detector (Vigo Systems, Poland) of 2–6 μm bandwidth through a pair of parabolic mirrors. A software lock-in amplifier (National Instruments, USA) demodulated the PTR signal from the detector and sent the amplitude and phase to the computer. A total of 59 data points were collected over the frequency range 60–2000 Hz in a logarithmic scale. To remove the instrumental effects, the measured demodulated PTR signals (A_s and P_s) were normalized by that from a reference sample (A_r and P_r), a bare steel substrate, before they were fitted to the foregoing theoretical model. For convenience, we henceforth refer to the normalized PTR signals, $A_n = A_s/A_r$, $P_n = P_s - P_r$, and denote the two channels A and P. The multi-parameter PTR fitting procedure was based on Eq. (4) with the Least Squares approach.

2. Theory validation

The separate parameter fitting method was validated by fitting the total coating thickness L ($= L_1 + L_2 = 1\times10^{-6}$ m $+ L_2$), together with the thermal diffusivity α_2 and thermal conductivity κ_2 as unknown parameters and comparing the fitted coating thickness with the measured one. Because the values of the thermal diffusivity and the thermal conductivity of the coating were not known through independent measurements, α_2, κ_2, and the related grouped parameters Q_2, P_2, and b_{32} are not used for validation, but their fitted values are

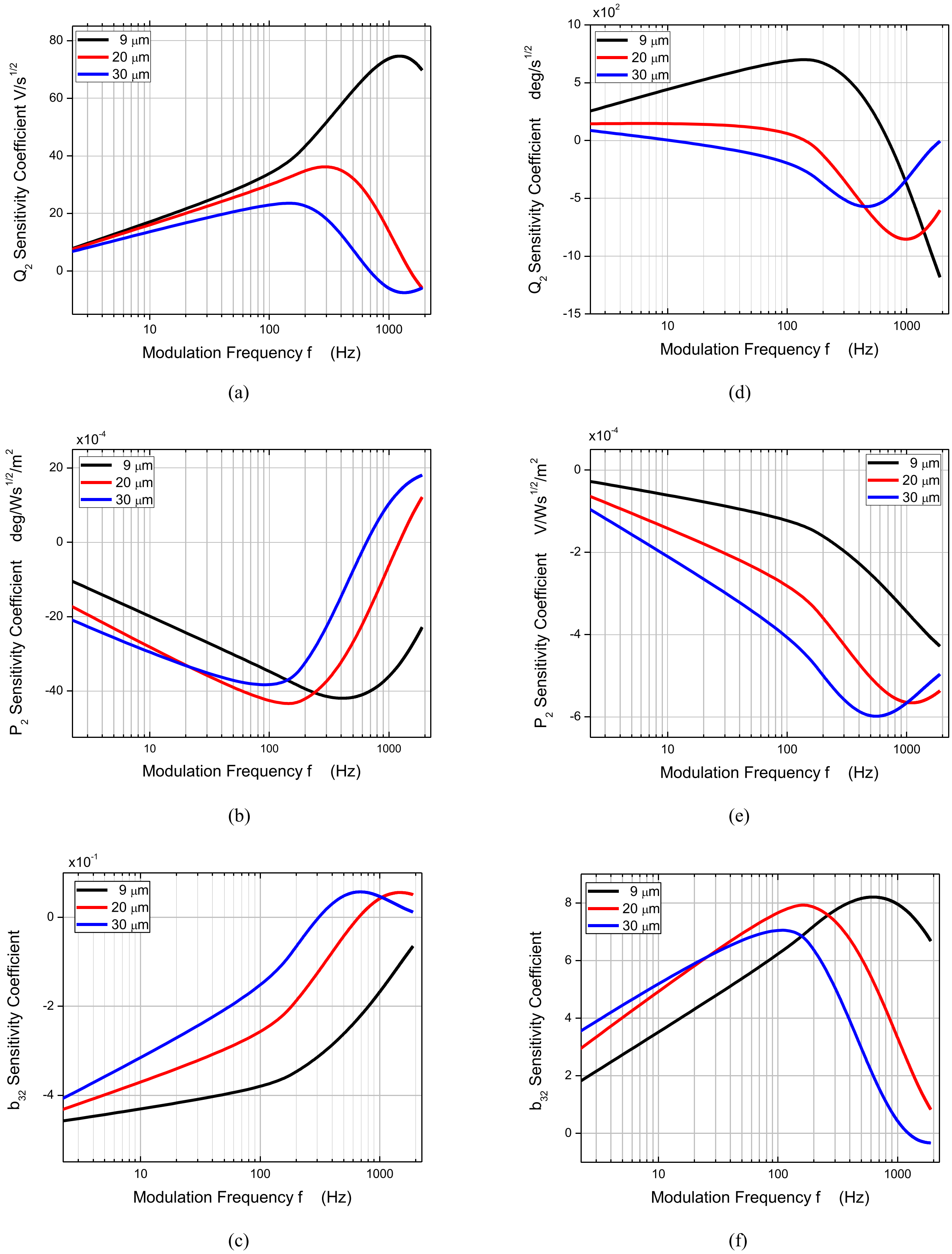

FIG. 10. Calculated grouped parameter sensitivity coefficients as functions of frequency f at three different coating thicknesses $L_2 = 9\,\mu$m, 20 μm, and 30 μm. Amplitude: (a) Q_2; (b) P_2; (c) b_{32}. Phase: (d) Q_2; (e) P_2; (f) b_{32}.

within the ranges listed in Table II. The best fits were performed using the full frequency range (60–2000 Hz, 59 data points) and also the optimal range (200–600 Hz, 19 points). The selection of the optimal amplitude range was based on the sensitivity coefficient plots in Fig. 5(c), which is optimal for both 20 μm and 9 μm coating thicknesses. Here only amplitude best fits to the data were shown to be optimal for validation because, as can be seen from Fig. 9(c) for 20 μm thickness, and Fig. 13 for 9 μm thickness, amplitude has an overall higher sensitivity than phase except for a few points at

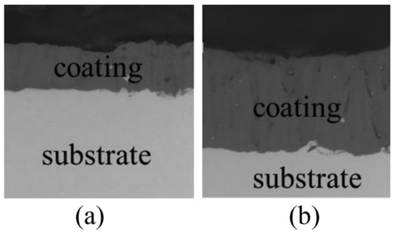

FIG. 11. Microscope images of cross-sections of coated sample with (a) 9.7 μm thick coating; (b) 20.6 μm thick coating.

the very high frequency end, while the 9 μm thickness phase exhibits zero sensitivity twice over the full frequency range. The compromised phase sensitivities in both figures are results of crossing over the zero sensitivity line so that the measurement of the phase, averaged over the relevant frequency range, cancels out the positive and negative contributions, thereby remaining in the immediate neighborhood of the zero crossing point, i.e., essentially being insensitive to parameter changes. The four fitted curves, two for the thin sample (full and optimal range) and two for the thick sample, are displayed in Fig. 14. The comparison between the data best fits and the measured L is presented in Table III (amplitudes) and Table IV (phases). For amplitudes, it is demonstrated that the L values of the thin sample (9.5 μm) and the thick sample (20.3 μm) fitted in the optimal range are well within the independently measured L error range ($9.7 \pm 0.78\,\mu$m and $20.6 \pm 0.63\,\mu$m). This result is significant for confirming the uniqueness of the measurement. In the full range fitting, the fitted L value of the thin sample (10 μm) remains within the measured L error, however the fitted L value of the thick sample (13.6 μm) is far away from the measured value. These results can also be understood from Fig. 5(c). For the 9 μm curve, the low sensitivity coefficient in the low frequency range is enhanced by its very high sensitivity values in the high frequency range, so that the overall (averaged) sensitivity is close to optimal. Figure 13 corroborates the source of sensitivity, showing that the amplitude response is high and flat up to ca. 600 Hz. So, results from "optimal" and "full" range for the 9.7-μm coating essentially coincide in Table III. For the 20 μm curve in Fig. 9(c), however, the average sensitivity is compromised away from the optimal range by the low and

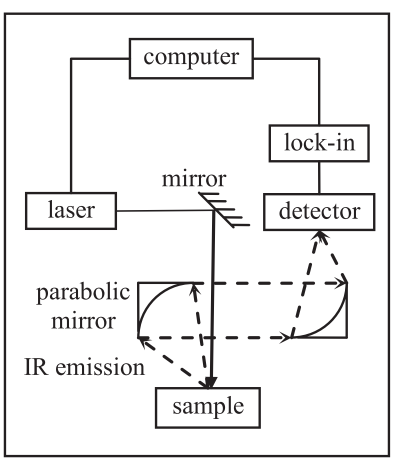

FIG. 12. Schematic diagram of PTR system.

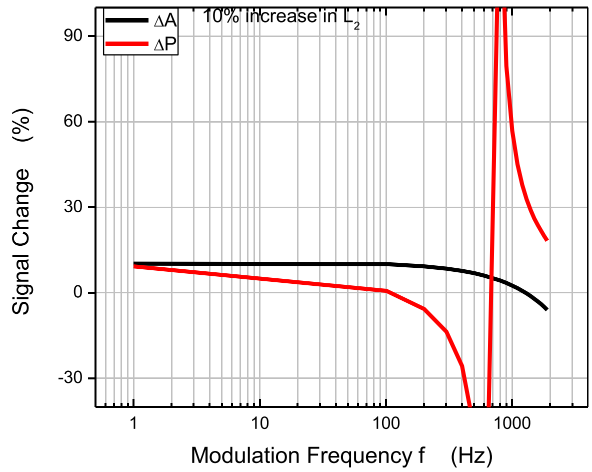

FIG. 13. Parameter sensitivity comparison between two signal channels, amplitude A and phase P, at $L_2 = 9\,\mu$m as a function of modulation frequency. Relative signal change, ΔA and ΔP, is due to 10% change in parameters L_2.

even negative sensitivity in the high frequency range which offsets the higher sensitivity in the low frequency range. This results in the twice zero-crossing amplitude as shown in Fig. 9(c). Thus the fitted L value is not reliable. However, the optimal frequency range, 200 – 600 Hz, corresponds to the highest sensitivity coefficient for $L_2 = 20\,\mu$m in Fig. 5(c), a fact rendering the L_2 measurement optimally reliable and well within the error of the actual independently measured thickness L_2. For comparison, the fitted L obtained with the phase data is presented in Table IV. It can be seen that, in general, the fitted L with phase data deviates more from the measured values, except for 20 μm in full range. For the 9.7-μm coating, it can be seen from Fig. 13 that the phase response crosses the zero line twice, one around 100 Hz (in both optimal and full ranges) and the other around 700 Hz (in full range). Thus the fitted values are not reliable in either optimal or full range. For the 20.6-μm coating, the phase response, Fig. 9(c), crosses the zero line for both optimal and full frequency ranges (60–200 Hz). This zero-crossing has a higher impact for the optimal range (fewer data points) than for the full range (more data points), The fitted thickness values, therefore, are more reliable from the full range fitting than from the optimal range fitting. In both cases, however, reliability is compromised due to the close proximity of the phase sensitivity coefficients to the zero line, compounded with positive and negative sensitivity cancellation upon averaging over the measurement frequency ranges. The net result is that the phase measurements are less reliable than the amplitude measurements, with the 9.7-μm coating measurement being less reliable than the 20.6-μm coating measurement. The above amplitude and phase fitting comparison implies that (1) the two signal channels have their own, often different, optimal ranges. Fitted parameters from the phase channel are not always more reliable than those from the amplitude channel, despite the prevailing notion among researchers that this is the case;[17,18] (2) the zero-crossing range must be avoided in parameter fittings because the closer the best fit around the zero-crossing region, the farther away the fitted values are from the real ones. The results of this case study quantified in Tables III and IV strongly suggest a major reason for the often observed

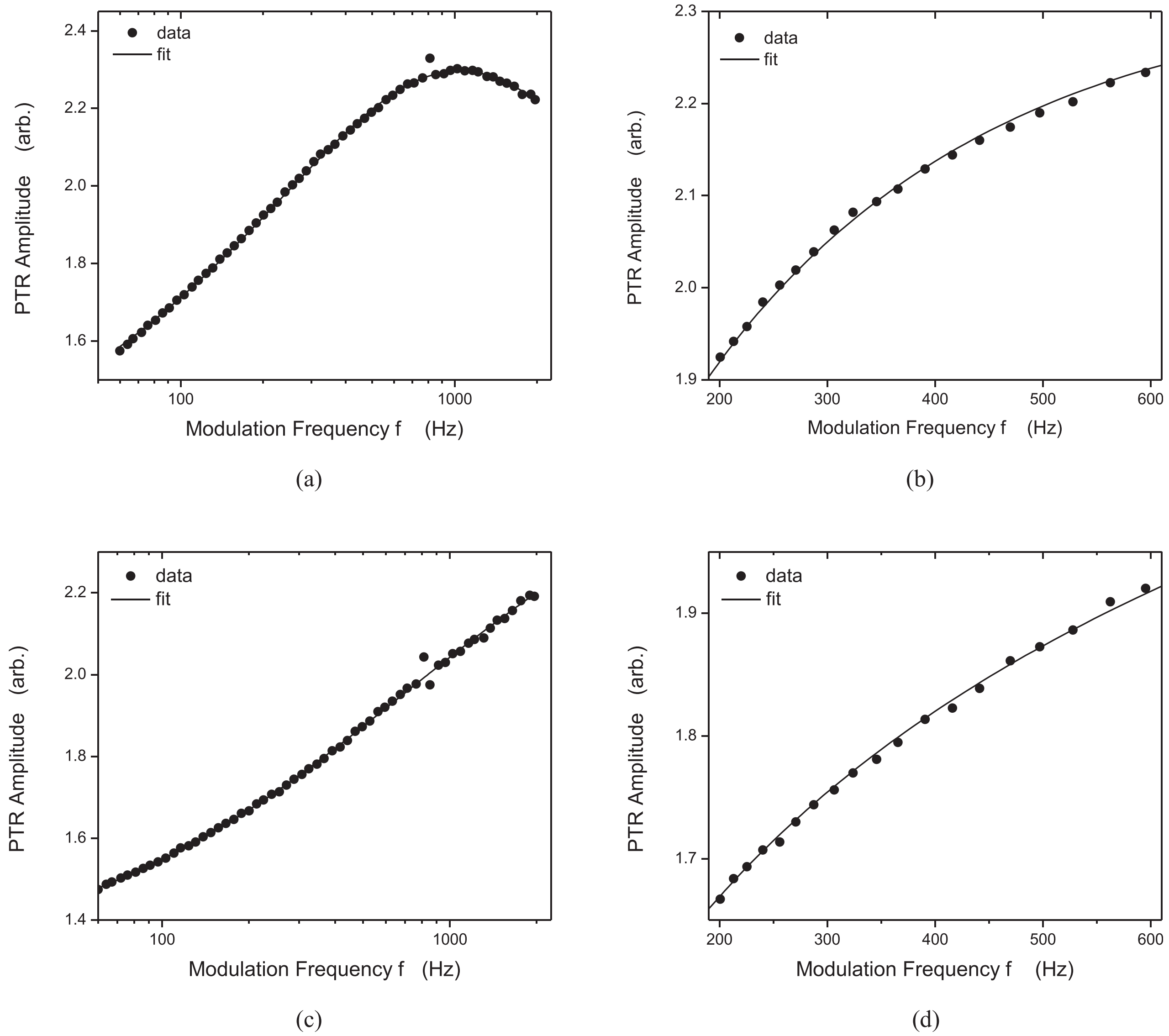

FIG. 14. The amplitude of two different coating thickness samples fitted in the full frequency range (60–2000 Hz) and in the optimal frequency range (200–600 Hz). (a) and (b): thick coating sample; (c) and (d): thin coating sample. The symbols are raw data and the lines are best fits.

discrepancy between thermal-wave measured parameters using best-fitted amplitude and phase data separately; a long standing puzzle with no identified cause or solution to-date, is the difference in sensitivities to those parameters when using a common frequency range. This underscores the usefulness and importance of generating sensitivity coefficient plots to determine the optimal amplitude and phase frequency ranges toward the achievement of reliable and self-consistent parameter measurements and identification of reliability criteria for the amplitude or the phase or both signal channels when used for thermophysical or thickness measurements.

TABLE III. Comparison between fitted and measured coating thickness (with amplitude data).

Estimation method	Fitting range	L_{thin} (m)	L_{thick} (m)
Fitted	Optimal range	9.5×10^{-6}	20.3×10^{-6}
	Full range	10.0×10^{-6}	13.6×10^{-6}
Measured		$(9.7 \pm 0.8) \times 10^{-6}$	$(2.06 \pm 0.06) \times 10^{-5}$

3. Procedural steps for application

Parameter identifiability analysis before any experiments is very important for reliable thermal-wave parameter measurements. Proper parameter measurement procedures should be as follows: (1) calculate the sensitivity coefficients of all the parameters based on the appropriate mathematical model; (2) check the identifiability of all the parameters based on the identifiability criteria, Section II B 2, resulting in maps like Figs. 2 and 3; (3) design the parameter extracting experiment within the proper independent variable range (e.g., frequency) where the parameters are identifiable and sensitive. The core

TABLE IV. Comparison between fitted and measured coating thickness (with phase data).

Estimation method	Fitting range	L_{thin} (m)	L_{thick} (m)
Fitted	Optimal range	14.3×10^{-6}	21.8×10^{-6}
	Full range	13.2×10^{-6}	20.9×10^{-6}
Measured		$(9.7 \pm 0.8) \times 10^{-6}$	$(2.06 \pm 0.06) \times 10^{-5}$

of the analysis of multi-parameter identifiability and sensitivity is to determine the sensitivity coefficients for all the possible values of parameters and independent variables. However, it is time consuming to compute such a large amount of data. There are some practical methods to simplify the calculations such as (1) putting feasible numerical limits to the range of parameters and independent variables as described; (2) using the Finite Difference Method (such as forward difference approximation) and the Sensitivity Equation Method (deriving sensitivity equations which can be solved separately from the model) [Ref. 12, Chap. 7, Sec. 7.10]; and (3) substituting sensitivity coefficients $\frac{\partial\eta_i}{\partial\beta_j}$ with relative sensitivity coefficients $\beta_j\frac{\partial\eta_i}{\partial\beta_j}$,[19] or $\frac{\beta_j}{\eta_i}\frac{\partial\eta_i}{\partial\beta_j}$,[15] because they can isolate parameters.

IV. CONCLUSIONS

We have introduced and investigated the concept of best-fitting reliability of a three-layer photothermal model to two ceramic coated steel samples of $\sim$9.7 μm and 20.6 μm coating thickness, respectively, using the parametric sensitivity theory. The theoretical fitting can either derive direct and separate thermal parameter values, or grouped parameters. Whether the fitted parameters are unique or not is determined by the identifiability criterion: the parameters are identifiable if their sensitivity coefficients are linearly independent over the range of the measurements. The linear independence of the sensitivity coefficients can be established by means of nonzero determinants of the sensitivity coefficient matrices. Sometimes, analytical expressions of the determinants may not be easy to derive. As an alternative, sensitivity coefficient plots are very useful and important in determining which parameters can be estimated reliably and, if they can be estimated, the magnitude of change of the response due to perturbations in the values of the parameters. Therefore, the experimental condition can be optimized based on the sensitivity coefficient plots. The reliability analysis theory is validated by comparing two independently measured coating thicknesses with best fitted values under random conditions (60–2000 Hz frequency range) and optimized conditions (200–600 Hz frequency range) and comparing the reliabilities of separate amplitude- and phase-based measurements with the help of the derived sensitivity coefficients.

ACKNOWLEDGMENTS

The financial support of the Natural Sciences and Engineering Research Council of Canada (NSERC) through an ENGAGE Grant to A.M. (2016) is thankfully acknowledged.

[1] P. E. Nordal and S. Kanstad, "Photothermal radiometry," Phys. Scr. **20**, 659–662 (1979).
[2] A. Tam and B. Sullivan, "Remote sensing applications of pulsed photothermal radiometry," Appl. Phys. Lett. **43**, 333–335 (1983).
[3] J. Spicer, W. Kerns, L. Aamodt, and J. Murphy, "Measurement of coating physical properties and detection of coating disbonds by time-resolved infrared radiometry," J. Nondestruct. Eval. **8**, 107–120 (1989).
[4] E. Welsch and D. Ristau, "Photothermal measurements on optical thin films," Appl. Opt. **34**, 7239–7253 (1995).
[5] J. Garcia, A. Mandelis, B. Farahbakhsh, C. Lebowitz, and L. Harris, "Thermophysical properties of thermal sprayed coatings on carbon steel substrates by photothermal radiometry," Int. J. Thermophys. **20**, 1587–1602 (1999).
[6] A. Kusiak, J. Martan, J. L. Battaglia, and R. Daniel, "Using pulsed and modulated photothermal radiometry to measure the thermal conductivity of thin films," Thermochim. Acta **556**, 1–5 (2013).
[7] N. Fleurence, B. Hay, G. Davée, A. Cappella, and E. Foulon, "Thermal conductivity measurements of thin films at high temperature modulated photothermal radiometry at LNE," Phys. Status Solidi **A**, 535–540 (2015).
[8] G. Busse and H. Walther, in *Progress in Photothermal and Photoacoustic Science and Technology, Vol. 1 Principles and Perspectives of Photothermal and Photoacoustic Phenomena*, edited by A. Mandelis (Elsevier, New York, 1992), Chap. 5, pp. 205–298.
[9] B. Bein and J. Pelzl, in *Plasma Diagnostics, Vol. II Surface Analysis and Interactions*, edited by O. Auciello and D. Flamm (Academic, New York, 1989), Chap. 6, pp. 211–326.
[10] C. Reyes, J. Jaarinen, L. Favro, P. Kuo, and R. Thomas, in *Review of Progress in Quantitative Nondestructive Evaluation*, edited by D. Thompson and D. Chimenti (Plenum, New York, 1987), Vol. 6A, Chap. 1, pp. 271–275.
[11] J. Hartikainen, J. Jarrinen, and M. Luukkala, "Microscopic thermal wave non-destructive testing," Adv. Opt. Electron. Microsc. **12**, 313–359 (1991).
[12] J. Beck and K. Arnold, *Parameter Estimation in Engineering and Science* (John Wiley & Sons, New York, 1977).
[13] C. Raudzis, F. Schatz, and D. Wharam, "Extending the 3ω method for thin-film analysis to high frequencies," J. Appl. Phys. **93**, 6050–6055 (2003).
[14] M. Bauer and P. Norris, "General bidirectional thermal characterization via the 3ω technique," Rev. Sci. Instrum. **85**, 064903 (2014).
[15] C. Jensen, M. Chirtoc, N. Horny, J. Antoniow, H. Pron, and H. Ban, "Thermal conductivity profile determination in proton-irradiated ZrC by spatial and frequency scanning thermal wave methods," J. Appl. Phys. **114**, 133509 (2013).
[16] A. Mandelis, *Diffusion-Wave Fields:* Mathematical Methods and Green Functions (Springer, New York, 2001).
[17] G. Langer, J. Hartmann, and M. Reichlinga, "Thermal conductivity of thin metallic films measured by photothermal profile analysis," Rev. Sci. Instrum. **68**, 1510–1513 (1997).
[18] F. Cernuschi, P. G. Bison, A. Figari, S. Marinetti, and E. Grinzato, "Thermal diffusivity measurements by photothermal and thermographic techniques," Int. J. Thermophys. **25**, 439–457 (2004).
[19] M. Ozisik and H. Orlande, *Invert Heat Transfer* (Taylor & Francis, New York, 2000).